
BAYESIAN SURFACE WARPING APPROACH FOR RECTIFYING GEOLOGICAL BOUNDARIES USING DISPLACEMENT LIKELIHOOD AND EVIDENCE FROM GEOCHEMICAL ASSAYS

A PREPRINT

**Raymond Leung*, Alexander Lowe,
Anna Chlingaryan, Arman Melkumyan, John Zigman**

Australian Centre for Field Robotics (ACFR)
Faculty of Engineering
The University of Sydney
Sydney, NSW 2006
raymond.leung@sydney.edu.au

April 1, 2021

ABSTRACT

This paper presents a Bayesian framework for manipulating mesh surfaces with the aim of improving the positional integrity of the geological boundaries that they seek to represent. The assumption is that these surfaces, created initially using sparse data, capture the global trend and provide a reasonable approximation of the stratigraphic, mineralization and other types of boundaries for mining exploration, but they are locally inaccurate at scales typically required for grade estimation. The proposed methodology makes local spatial corrections automatically to maximize the agreement between the modelled surfaces and observed samples. Where possible, vertices on a mesh surface are moved to provide a clear delineation, for instance, between ore and waste material across the boundary based on spatial and compositional analysis; using assay measurements collected from densely spaced, geo-registered blast holes. The maximum a posteriori (MAP) solution ultimately considers the chemistry observation likelihood in a given domain. Furthermore, it is guided by an apriori spatial structure which embeds geological domain knowledge and determines the likelihood of a displacement estimate. The results demonstrate that increasing surface fidelity can significantly improve grade estimation performance based on large-scale model validation.

Keywords Geochemistry-based Bayesian deformable surface (GC-BDS) model · Bayesian Computation · Mesh Geometry · Surface Warping · Spatial Correction · Displacement Likelihood · Geological Boundaries · Model Integrity.

CCS Concepts:

- Computing methodologies → Mesh geometry models;
- Mathematics of computing → Bayesian computation;
- Applied computing → Earth and atmospheric sciences.

*Corresponding author. All authors are affiliated with the Rio Tinto Centre for Mine Automation and work in ACFR at The University of Sydney.

1 Introduction

Spatial structures and spatial algorithms are sometimes overshadowed by geostatistics and geochemical analysis in geology and stratigraphic modelling despite playing a no-less important role. In this paper, *surface warping* is concerned with computational methods for mesh surface manipulation that automatically increase spatial fidelity [1].² Specifically, it focuses on reshaping and correcting inaccuracies in an existing surface to maximize its agreement with observed data; in particular, geochemical assays sampled from drilled holes in an ore deposit.

For decades, displacement field estimation (e.g. [3][4][5][6][7]) and surface editing techniques (e.g. [8][9]) have flourished in the computer vision and computer graphics community. The idea of directly manipulating mesh surface vertices can be traced back to Allan, Wyvill and Witten [10] amongst others in a contemporary context, where the concepts of region of influence, movement constraints (in terms of decay function, bound and anchored vertices) are discussed.

In specific disciplines such as video coding, dense motion field (optical flow) estimation and segmentation have, for instance, been attempted using deformable mesh motion models and MAP estimators. The a priori distribution of the estimates can be modelled by a coupled Markov random field to account for both spatial smoothness and temporal continuity along the estimated motion trajectories [11]. Despite these similarities, the *surface and boundary alignment* problem considered in this paper differs in some significant ways. Although displacement estimation remains a central theme, the observations rely on *geochemistry* rather than photogrammetry (or interferometry in the case of strain tensor estimation from geodetic and satellite deformation measurements [1]) and these observations are sparse, spatially irregular and noisy in comparison.

For the surface and boundary alignment problem, mesh processing techniques [12] and domain knowledge [13] can play a crucial role. To the authors' knowledge, *displacement field estimation* has not been utilized previously in 3D surface-based modelling of geological structures [14] or exploited in practice to improve the efficacy of models in mining. This paper aims to bridge the gap that exists between a model and the latest data acquired from a mine. The Bayesian approach basically connects a model (or belief) with evidence from geochemical observations (the reality). Displacement estimation helps identify discrepancies, then surface warping corrects spatial inaccuracies in the surface-based representation of the relevant geological structures.

In the literature, research has progressed largely in two separate streams: (1) advances in computational techniques that manipulate surfaces using dense uniformly sampled data, where warping is used to process visual information or register anatomical changes via MRI [15] for instance; (2) generating 3D subsurface models using extensive field data and different modalities, a variety of techniques (including the use of contours and differential geometry) are summarized in [16] (Sect. 1.1) and [14].

In the first research stream, examples include (a) energy constrained mesh deformation using subspace gradient domain techniques [17] where the targeted application is computer animation; and (b) post-rendering 3D warping which compensates for occlusion-related artifacts due to viewpoint variation by compositing interpolants from multiple reference frames [5]. In computer graphics, methods for constructing extrinsically smooth and globally optimal directional fields have been considered by Jakob et al. [18], Huang and Ju [19] and Knöppel et al. [20] where it is treated as a discrete optimization or sparse eigenvalue problem.

An example from the second stream is the work of Olierook et al. [21] which uses a Bayesian approach to fuse lithostratigraphic field observations with aeromagnetic and gravity measurements to build 3D geological models without structural data. Such model is fit for purpose for mineral exploration; however the grade control requirements encountered in a mine production setting are generally more stringent and demands far greater precision and vertical resolution. In [22], Calcagno et al. use cokriging [23] to create a continuous 3D potential field to describe the geometry of the geology. The model input consists of the location of geological interfaces and orientation data. Subsequently, structural information such as the location and orientation of boundaries are extracted from isosurfaces and the gradient of the interpolated potential function.

The state of the art [24] generally considers modelling as an open-loop process where the input data is complete and a static model is to be produced. In practice, data is usually harvested bench-by-bench in a piecemeal manner in open-pit mining. Thus, there is a strong incentive in utilizing newly acquired data to improve both surface definitions and the existing model, to further understand the subterranean deposit below the current bench for mine planning and operational guidance.

²This should not be confused with alternative meanings in geomorphology for instance where *surface warping* is attributed to cross-bending stresses resulting from torsional forces in the study of the mechanics of geologic structures [2].

The missing link is a synergy between geochemical data, surface representation and the model — and whether grade prediction performance can benefit from an incremental update strategy. These novel issues have not received much attention in earth and spatial science. In terms of where this paradigm fits, based on Nealen’s survey article [8], a new category called geochemistry-based Bayesian deformable surface (GC-BDS) model is proposed to characterize the warping approach presented in this paper.

1.1 Motivation

To understand the importance of surface and boundary alignment, we first consider the implications of working with an inaccurate (or misleading) surface and its flow-on effects on subsequent modelling processes before formulating a Bayesian framework for surface warping with a view of improving surface integrity. As motivation, we illustrate how starting with a bad surface — one that is not representative of the true geological boundary — can impact on the block structure and inferencing ability of a grade estimation model.

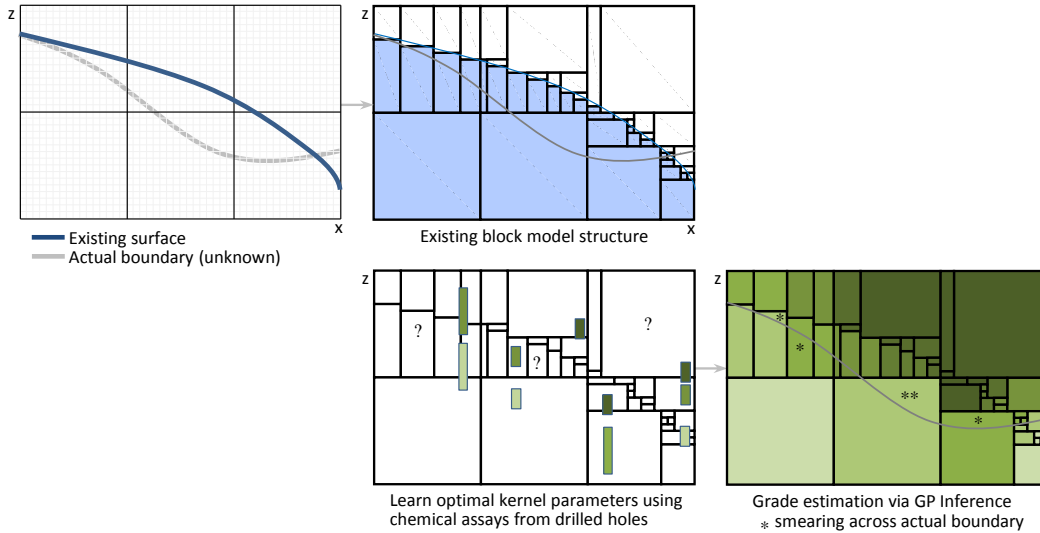


Figure 1: Computational pipeline for the orebody grade estimation task. Block model spatial restructuring and inferencing both suffer from the negative effects of a surface that misrepresents the true geological boundary. The question marks serve as a reminder that the grade value of all the blocks need to be estimated.

Figure 1 illustrates the computational pipeline for a typical grade estimation problem where the main objectives are (i) obtain a compact block-based representation of the orebody with good boundary localization property; (ii) estimate the grade value for chemical components of interest, predicting these values especially at locations where no measurements are available using geostatistical or machine learning techniques. For the first objective, it requires changing the spatial structure of the model, partitioning the blocks as necessary (down to some predetermined, acceptable minimum block size) to closely follow the location and approximate the curvature of the geological boundary which the surface seeks to represent. In Fig. 1(top middle), we have a situation where the existing surface misrepresents the location of the actual boundary [which is not directly observable].³

Consequently, the spatial restructuring algorithm [25] produces a block structure that is not faithful to the underlying boundary through no fault of its own. For the second objective, using a Gaussian Process (GP) learning and inferencing approach [described in Appendix A], spatial variations (covariance functions) are learnt using samples drawn from an incorrect geological domain structure. A major consequence, depicted in Fig. 1(bottom right), is that the inferred values for the blocks are biased near the actual boundary due to under-estimation or over-estimation of the chemistry values, and the blocks not properly decomposed to follow the shape of the boundary. These two factors lead to smearing in the predicted chemistry across the actual boundary which has practical implications for ore extraction and material blending in a production setting.

The main proposition of this paper is a Bayesian approach that corrects inaccuracies in a mesh surface through spatial warping which thus increases the positional integrity of the underlying boundary that it seeks to represent. Conceptually, the problem involves estimating the displacements to bring an existing surface into alignment with the true boundary

³For illustrative purpose, Fig. 1 shows a situation where the modelled boundary is grossly misplaced. In practice, the discrepancies that exist between the actual and initial modelled boundary are often explained by local differences due to inadequate sampling.

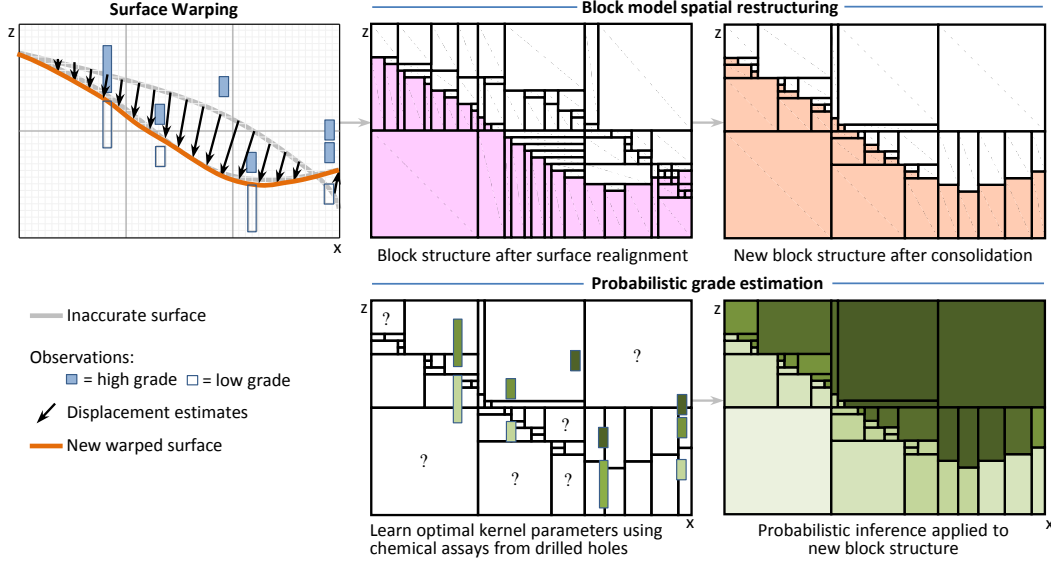


Figure 2: Rectification of the boundary through surface warping improves the spatial structure and inferencing ability of the grade block model.

based on the observed sample chemistry. The aim is to capture more precisely the shape and location of local features; this is depicted in Fig. 2(top left). The existing block structure is modified adaptively to align itself with the new warped surface. In Fig. 2(top center), the new block structure evidently follows the curvature of the new surface, however some of the preexisting (subdivided) blocks from the earlier misplaced boundary still remain. A block merging algorithm proposed in [25] is used to coalesce fragmented blocks to produce the consolidated block structure shown in Fig. 2(top right). The GP inferencing procedure is applied once again to the new block structure. The result shown in Fig. 2(bottom right) is free of blending or smearing artefacts. When the surface is accurate, the resultant model exhibits a clear contrast in the predicted grade values on either side of the actual boundary. Improving the reliability of these estimates ultimately enables better decision making, planning and ore extraction.

To summarise, an ill-placed boundary can impact the block structure and grade estimation in significant ways. The boundary localization properties deteriorate when a block model is partitioned by an inaccurate surface. Incorrect geological domain classification resulting from a misleading surface can cause smearing to occur during inferencing where compositions are over-estimated or under-estimated near the actual boundary.

1.2 Contributions

In Section 2, the surface warping problem is formulated in a Bayesian framework and the MAP (maximum a posteriori) solution for node displacements estimation is presented; this serves to maximize the agreement between surfaces and geochemical observations from blast hole samples. In Section 3, local improvements are visually highlighted. An objective measure called r_2 *cdf error score* is proposed and used for model validation to demonstrate an improvement in grade estimation performance resulting from spatial warping.

2 Surface warping

Surface warping may be framed as a Bayesian parametric inference problem where the objective is to estimate the required displacements (or spatial corrections) $\theta \equiv \mathbf{d} \in \mathbb{R}^3$ to maximize the positional integrity of geological boundaries given a set of observations. In general terms, the observations consist of the location $\mathbf{x} \in \mathbb{R}^3$ and spatial extent $\delta = [0, 0, h]^T \subseteq \mathbb{R}^3$ of the measurements, as well as the composition $\mathbf{c} \in \mathbb{R}^K$ of the sample determined by chemical assays. The prior information available is a reference geological structure \mathcal{G} that determines the geozone classification ($g \in \mathbb{Z}$) of a sample which indicates the geological domain where it belongs. This prior embeds knowledge about the stratigraphic structure of the modelled region which is considered a faithful (unbiased) representation of the ground truth at large scales, but inaccurate at smaller scales ($\sim 5 - 20\text{m}$) due to sparse sampling and local variation.

Accordingly, applying Bayes rule, the problem may be formulated as

$$\arg \max_{\mathbf{d}} P(\mathbf{d} | \mathbf{c}, \mathbf{s}) \quad (1)$$

where spatial information is contained in $\mathbf{s} = [\mathbf{x}, \boldsymbol{\delta}]^T \in \mathbb{R}^6$ and

$$P(\mathbf{d} | \mathbf{c}, \mathbf{s}) \propto P(\mathbf{c} | \mathbf{d}, \mathbf{s}) P(\mathbf{d} | \mathbf{s}) \quad (2)$$

$$= \left(\sum_g P(\mathbf{c}, g | \mathbf{d}, \mathbf{s}) \right) P(\mathbf{d} | \mathbf{s}) \quad (3)$$

$$= \left(\sum_g P(\mathbf{c} | g, \mathbf{d}, \mathbf{s}) P(g | \mathbf{d}, \mathbf{s}) \right) P(\mathbf{d} | \mathbf{s}) \quad (4)$$

$$= \sum_g P(\mathbf{c} | g, \mathbf{d}, \mathbf{s}) P(g | \mathbf{d}, \mathbf{s}) P(\mathbf{d} | \mathbf{s}) \quad (5)$$

$$\approx \sum_g P(\mathbf{c} | g) P(g, \mathbf{d} | \mathbf{s}) \quad (6)$$

Marginalization, conditional probabilities and conditional independence,⁴ ($\mathbf{c} \perp\!\!\!\perp \mathbf{d}, \mathbf{s} \mid g$), are used in (3), (4) and (6), respectively. The final expression in (6) offers a clear interpretation for the posterior $P(\mathbf{d} | \mathbf{c}, \mathbf{s})$. Specifically, $P(\mathbf{c} | g)$ denotes the likelihood of observing the chemical composition \mathbf{c} in geozone g , whereas $P(g, \mathbf{d} | \mathbf{s})$ represents a spatial prior that considers the displacement and geozone likelihood given the sample location. This Bayesian network is described by the graphical model shown in Fig. 3. Even for this simple structure, there is tremendous scope for ingenuity. The following describes one possible implementation and reflects on some practical issues.

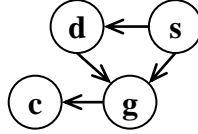


Figure 3: Graphical model for surface warping. The graph expresses the conditional dependence structure between the random variables: \mathbf{c} =observed chemistry, \mathbf{g} =geozone, \mathbf{d} =displacement and \mathbf{s} =spatial properties. The arrows represent conditional dependency of a target node from a source node.

For readers new to geostatistics, a common pitfall is an attempt to model $P(\mathbf{c} | g)$ directly using raw chemical assay measurements and an affinity measure such as the Mahalanobis distance, $d^2(\mathbf{c}^{\text{sample}}, \mathbf{c}^{\text{class}})$. As Filzmoser et al.[26] have pointed out, statistical analysis performed on compositional data⁵ without resorting to log-ratio transformation may lead to invalid or dubious interpretations [27]. Even when the Mahalanobis distance metric can be legitimately applied following isometric log-ratio transformation [28], it may still be inappropriate, as errors of the same magnitude may have different levels of significance depending on the grading thresholds. In grade estimation work, samples are routinely categorized based on composition. Thus, instead of $P(\mathbf{c} | g)$, a likelihood probability mass function $L(y(\mathbf{c}) | g)$ is used by Lowe in [29] where $y(\mathbf{c})$ represents a categorical label. These labels generally correspond to mineralogical groupings or ‘destination tags’ since the excavated materials will be sorted eventually based on chemical and material properties.⁶

In practice, there is a finite number of mineralogical groupings and geozones. Hence, $L(y(\mathbf{c}) | g)$ is computed from a table with dimensions $(N_{\text{class}}, N_{\text{geozone}})$ constructed using frequency counts applied to assay samples collected from exploration drillings. Here, \mathbf{c} is observed, $y(\mathbf{c}) : \mathbb{R}^K \rightarrow \mathbb{Z}$ is a deterministic mapping and g is known.

⁴In our experience, using $p(\mathbf{c} | g, \mathbf{d}, \mathbf{s})$ does not further increase performance since spatial attributes are already modelled by $P(g, \mathbf{d} | \mathbf{s})$.

⁵A key characteristic of compositional data is that they lie in the Aitchison Simplex [26], which means the data is not Gaussian (or even symmetrically) distributed. An increase in a key component may cause another to decrease and the components sum to a constant.

⁶For downstream ore processing, it is useful to know whether the material is hard or friable, lumpy or fine, viscous or powdery. Typically, 6 to 12 categorical labels, $y(\mathbf{c})$, are used. For our purpose, we focus more on sample chemistry. The criteria for HG (high grade) and LGA (low grade aluminous) iron ore, for instance, might be set at $\text{Fe} \geq 60\%$ and $(50\% \leq \text{Fe} < 60\%, \text{Al}_2\text{O}_3 \geq 3\%)$, respectively. These parameters vary depending on the deposit and geozone.

For the prior $P(g, \mathbf{d} | \mathbf{s}(\mathbf{x}, \delta))$, a proxy function $R(\mathbf{x} + \mathbf{d}, g, \delta)$ is used to compute the geozone and displacement likelihood in [29]. This utilizes the a priori geological structure \mathcal{G} to assess the feasibility of displacement \mathbf{d} . In particular, $R(\mathbf{x} + \mathbf{d}, g, \delta)$ determines the amount of overlap, $r \in [0, 1]$, between geozone g and an interval observation δ of length h at the proposed location $(\mathbf{x} + \mathbf{d})$. Alternatively, spatial correlation may be modelled using autocorrelation functions and random field simulation as demonstrated in [30] in regions where stratigraphic association can be reasonably inferred from dense drill hole samples. It is clear that a number of strategies can be used to find the optimal displacement in a hierarchical search space. For instance, a conditional random field may be used to impose connectivity and regularization constraints. For simplicity and speed, a set of candidate displacement points $\{\mathbf{d}_i\}$ may be chosen from a regular 3-D lattice in the vicinity of \mathbf{x} , viz., $\mathcal{L}_{\mathbf{x}}$. Assuming $|\mathcal{L}_{\mathbf{x}}| = N_{\text{displacement}}$ for all \mathbf{x} , the posterior would result in a table of size $(N_{\text{sample}}, N_{\text{displacement}})$. The maximum a posteriori (MAP) estimate is given by (7), the solution with minimum $\|\mathbf{d}\|$ is chosen in the event of a tie.

$$\begin{aligned} \mathbf{d}_{\text{MAP}}(\mathbf{x}) &= \arg \max_{\mathbf{d}} L(\mathbf{d} | y(\mathbf{c}), \mathbf{s}(\mathbf{x}, \delta)) \\ &= \arg \max_{\mathbf{d}} \sum_g L(y(\mathbf{c}) | g) R(\mathbf{x} + \mathbf{d}, g, \delta) \end{aligned} \quad (7)$$

Diffusion flow techniques (based on using discrete Laplace-Beltrami [12]) may be applied to manifold surfaces to obtain a coherent displacement field where $\mathbf{d}_{\text{MAP}}(\mathbf{x})$ varies smoothly. However, dithering often presents as a simpler alternative. The solution is obtained as an aggregate average over a small neighbourhood, $\{\mathbf{x} + \epsilon_i\} \in \mathcal{N}_{\mathbf{x}}$,⁷ with higher weights $w(\mathbf{x}_i)$ given to nearby estimates and displacements perpendicular to the surface normal $\mathbf{n}_{\mathbf{x}}$.

$$\mathbf{d}'_{\text{MAP}}(\mathbf{x}) = \sum_{\mathbf{x}_i \in \mathcal{N}_{\mathbf{x}}} w(\mathbf{x}_i) \cdot \mathbf{d}_{\text{MAP}}(\mathbf{x}_i) \quad (8)$$

For instance, setting $w(\mathbf{x}_i)$ to $\text{proximity}(\mathbf{x}, \mathbf{x}_i) \times |\langle \mathbf{n}_{\mathbf{x}}, \mathbf{d}_{\text{MAP}}(\mathbf{x}_i) \rangle|$ provides local smoothing and discourages movement parallel⁸ to the surface which is not productive.⁹ In instances where stratigraphic forward modelling (SFM) hints are available, $\mathbf{n}_{\mathbf{x}}$ may be guided instead by directional projections based on the deposition and evolution of sedimentary facies within a stratigraphic framework [31]. Given a set of mesh surface vertices $\mathbf{x}_q \in \mathcal{S}$, their corrected positions after surface warping are given by

$$\mathbf{x}'_q = \mathbf{x}_q - \mathbf{d}'_{\text{MAP}}(\mathbf{x}_q). \quad (9)$$

Equation (9) simply applies the displacement-error corrections to surface vertices.

Computing this expression usually requires spatial interpolation as $\mathbf{d}_{\text{MAP}}(\mathbf{x})$ is initially evaluated at sparse locations where assay information (geochemical evidence) is available. In areas where spatial resolution is low, mesh surface triangles may be subdivided to increase point density. The classification function, $y(\mathbf{c}) : \mathbb{R}^K \rightarrow \mathbb{Z}$, and more generally $p(\mathbf{c} | g)$, may be learned [32] using supervised or unsupervised techniques when the rules for destination tags (mineralogical grouping) are inadequate or unavailable.

2.1 Algorithm

The Bayesian surface warping algorithm may be summarised in a series of steps. The description here is immediately followed with explanation and illustration of the key steps in Sec. 2.2.

Given a chemical assay to material type categorical mapping $y(\mathbf{c}) : \mathbb{R}^K \rightarrow \mathbb{Z}$,

1. Compute $L(y(\mathbf{c}) | g) \in \mathbb{R}^{N_{\text{class}} \times N_{\text{geozone}}}$ using training samples $\{(\mathbf{c}_j, g_j)\}_j$ from exploration holes

For each blast hole sample $i = 1, \dots, N_{\text{sample}}$:

2. Assign categorical label $y(\mathbf{c}_i) \in \{1, \dots, N_{\text{class}}\}$ to each sample
3. Compute $L(y(\mathbf{c}_i) | g)$ across all N_{geozone} geozones
4. Compute geozone-displacement likelihood, $R(\mathbf{x}_i + \mathbf{d}_i, g, \delta_i)$

For each surface vertex \mathbf{x}_q and candidate displacement vector \mathbf{d}_k from $\mathcal{L}_{\mathbf{x}_q}$, $k \in \{1, \dots, N_{\text{displacement}}\}$:

5. Interpolate the displacement field

(a) Find the M nearest¹⁰ samples to \mathbf{x}_q

⁷ Another option is to treat $\mathcal{N}_{\mathbf{x}}$ as the barycentric cell or mixed Voronoi cell [12] in the 1-ring neighbourhood of \mathbf{x} .

⁸ Tangential movements do not effectively compensate for displacement errors which are perpendicular to the surface.

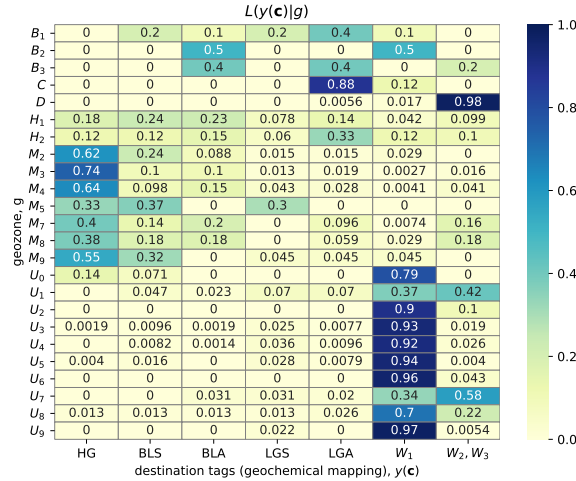
⁹ In our implementation, IDW (inverse distance weights) are used for $\text{proximity}(\mathbf{x}, \mathbf{x}_i)$. Another option is to use normalized exponential (softmax) function $\frac{e^{-\beta z_i}}{\sum_{i \in \mathcal{N}} e^{-\beta z_i}}$ where $z_i = \|\mathbf{x} - \mathbf{x}_i\|$. For the direction penalty term, $1 - (1 - \cos^2 \theta)^2$ is used in place of $|\langle \mathbf{n}_{\mathbf{x}}, \mathbf{d}_{\text{MAP}}(\mathbf{x}_i) \rangle|$, where $\cos \theta = \langle \mathbf{n}_{\mathbf{x}}, \mathbf{d}_{\text{MAP}}(\mathbf{x}_i) \rangle$.

¹⁰ Alternatively, use samples inside a local geodesic ball, e.g. within the 1-ring neighbourhood [12].

- (b) Compute $L_{m,k} \equiv L(\mathbf{d}_{m,k} | y(\mathbf{c}_m), \mathbf{s}_m(\mathbf{x}_m, \delta_m)) = \sum_g L(y(\mathbf{c}_m) | g) R(\mathbf{x}_m + \mathbf{d}_{m,k}, g, \delta_m)$ to obtain a table where $m \in \{1, \dots, M\}$ and $k \in \{1, \dots, N_{\text{displacement}}\}$.
- (c) Normalize each row s.t. $\max_k L(\mathbf{d}_{m,k} | y(\mathbf{c}_m), \mathbf{s}_m(\mathbf{x}_m, \delta_m)) = 1$ for each m
- (d) Compute weights incorporating proximity and directional preference:
 $w_{m,k}(\mathbf{x}_q) \propto \text{proximity}(\mathbf{x}_q, \mathbf{x}_m) \times |\langle \mathbf{n}_{\mathbf{x}_q}, \mathbf{d}_{m,k} \rangle|$ and $\sum w_{m,k} = 1$
- (e) Compute $\bar{L}(\mathbf{d}_k | y(\mathbf{c}_m), \mathbf{s}_m) = \sum_m w_{m,k} L_{m,k}$
- (f) Let $\mathbf{d}_{\text{MAP}}(\mathbf{x}_q) = \mathbf{d}_{m,k^*}$ where $k^* = \arg \max_k \bar{L}(\mathbf{d}_k | y(\mathbf{c}_m), \mathbf{s}_m)$
6. Apply smoothing to MAP displacement estimate. For example,
 - (a) Compute inverse distance weights $w_{p,q}$ for neighbour points $\mathbf{x}_p \in \mathcal{N}_{\mathbf{x}_q}$ s.t. $\sum w_{p,q} = 1$
 - (b) Compute $\mathbf{d}'_{\text{MAP}}(\mathbf{x}_q) = \sum_p w_{p,q} \cdot \mathbf{d}_{\text{MAP}}(\mathbf{x}_p)$
7. Apply correction to surface vertex to minimize discrepancy
 - (a) Update $\mathbf{x}'_q \leftarrow \mathbf{x}_q - \mathbf{d}'_{\text{MAP}}(\mathbf{x}_q)$
8. Post-processing step: resolve conflicts, e.g. any surface patch intersection that may arise.

2.2 Illustration

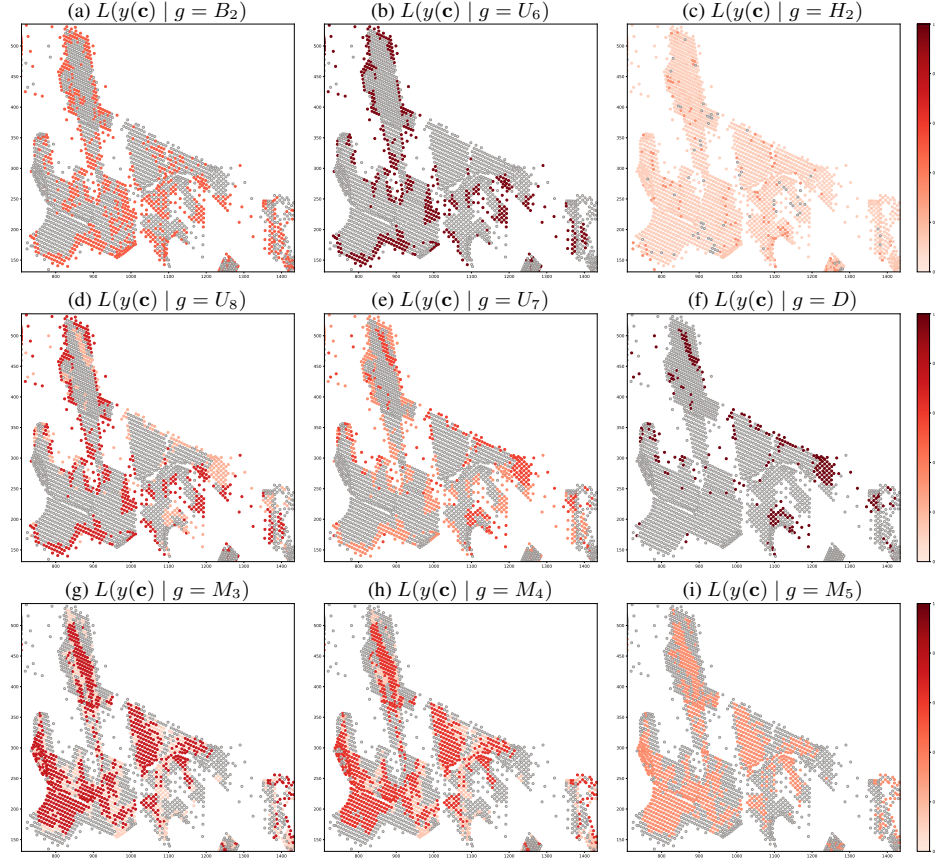
The Algorithm presented in Sec. 2.1 step 1 produces a table for $L(y(\mathbf{c}) | g)$. The example shown in Fig. 4 has size $N_{\text{geozone}} = 24$, $N_{\text{class}} = 7$. The exact definitions and geochemical mapping, $y(\mathbf{c})$, used will vary depending on the site. The main point to convey is the probabilistic association between chemistry and geozone, thus an assay sample with destination tag $y(\mathbf{c})$ has a plausible connection with multiple geozones in general. For instance, the HG tag has strong affinity with mineralized geozones (M) but its association with hydrated domains (H) cannot be discounted based on chemical evidence alone. This multivalent proposition is emphasized in Fig. 5 where each dot corresponds to a single blasthole assay observation $y(\mathbf{c}_i)$ (computed in step 2) and often a given location lit up in multiple geozones across different panels. This represents a spatial description of the evaluation in step 3. The panels in Fig. 5 reveal spatial correlation with certain orebody structures and varying response (probability) associated with the dolerite dyke (D) in row 2 and mineralized geozones (M) in row 3.



Destination definitions — HG (high grade): $\text{Fe} \geq 60$ and $\text{Al}_2\text{O}_3 < 6$, BL (blended): $\text{Fe} \in [55, 60]$, LG (low grade): $\text{Fe} < 55$;
 +S (siliceous: $\text{Al}_2\text{O}_3 < 3$), +A (aluminous: $\text{Al}_2\text{O}_3 \in [3, 6]$), W_1 (waste: $\text{Fe} < 50$ and $\text{Al}_2\text{O}_3 < 6$), $W_{2,3}$ (waste: $\text{Al}_2\text{O}_3 \geq 6$)
 Geozone definitions: H =hydrated, M =mineralized, U =unmineralized, C =canga, B =detrital, D =dolerite.

Figure 4: Likelihood table of destination tag (geochemical mapping) given geozone, $L(y(\mathbf{c}) | g)$

Step 4 of the algorithm starts incorporating spatial information to disambiguate between geozone candidates whose chemistry are consistent with the observed assay sample. In concert, step 5 performs displacement estimation to minimize geochemical discrepancies with respect to the existing boundary represented by the surface. Fig. 6 provides a motivating example for both endeavors. First of all, if an assay sample is chemically consistent with the geozone it



Geozone designations: H =hydrated, M =mineralized, U =unmineralized, D =dolerite, B =detrital/other categories

Figure 5: Evaluation of $L(y(\mathbf{c}_i) | g)$ across geozones for many samples \mathbf{c}_i within a spatial region of interest

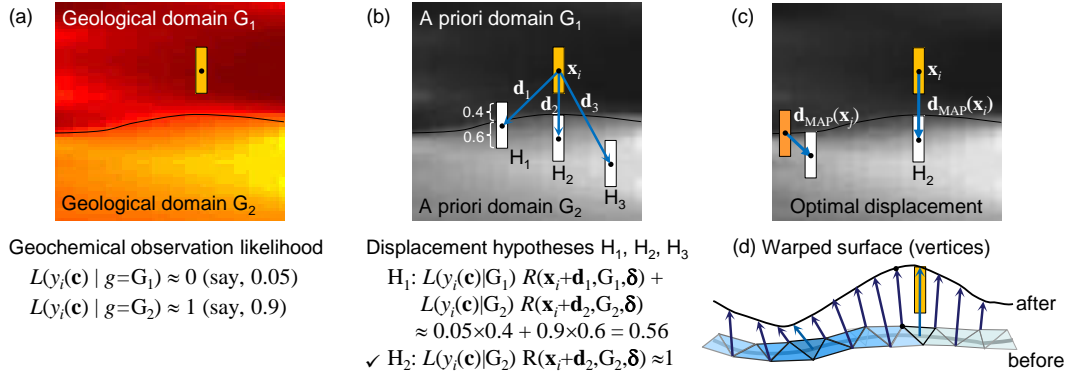


Figure 6: Displacement estimation using $L(y(\mathbf{c}_i) | g)R(\mathbf{x}_i + \mathbf{d}_i, g, \delta_i)$

is currently situated in, there is no need for any spatial correction. It is only required when the observed chemistry is incongruent with the geochemical characteristics of the assumed domain at the measured location.

Figure 6(a) shows an out-of-place (low grade Fe) observation within a mineralized domain. This is reflected numerically by $L(y(\mathbf{c}_i) | G_1) \ll L(y(\mathbf{c}_i) | G_2)$, where $G_1 \in M$ and $G_2 \in U$ belong to mineralized and unmineralized domains, respectively. Fig. 6(b) elaborates on step 5b: $L_{m,k} \equiv L(\mathbf{d}_{m,k} | y(\mathbf{c}_m), \mathbf{s}_m(\mathbf{x}_m, \delta_m))$ for just one sample ($m = 1$) and considers three displacement hypotheses H_k with displacement vectors $\mathbf{d}_k \equiv \mathbf{d}_{m,k}$, $k \in \{1, \dots, K\}$ where $K = 3$. The geozone-displacement likelihood $R(\mathbf{x}_m + \mathbf{d}_{m,k}, g, \delta_m)$ is determined by the fraction of sample interval overlap with the a priori geozone structure. The example in Fig. 6(b) shows the displacement hypothesis H_2 has the greatest support numerically. Intuitively, it represents the translation required to move the low grade sample completely into the

unmineralized domain, G_2 . Although hypothesis H_3 also provides a feasible solution, the displacement is greater and therefore it is not preferred.

Based on these principles, Fig. 6(c) shows the optimal displacement estimated for $M = 2$ samples. Put simply, step 5e roughly corresponds to Fig. 6(d) where the displacement computed for a surface vertex \mathbf{x}_q is essentially a weighted average of the estimated displacement from its M nearest neighbors. Step 6 typically produces a locally smooth displacement error field. For an arbitrary vertex \mathbf{x}_q , the optimal solution, $\mathbf{d}'_{\text{MAP}}(\mathbf{x}_q)$, appears as a peak (see asterisk) in the parameter space in Fig. 7. Finally, the surface vertices are adjusted to complete step 7, this may be seen as additional smoothing or extrapolation on top of Fig. 6(d).¹¹

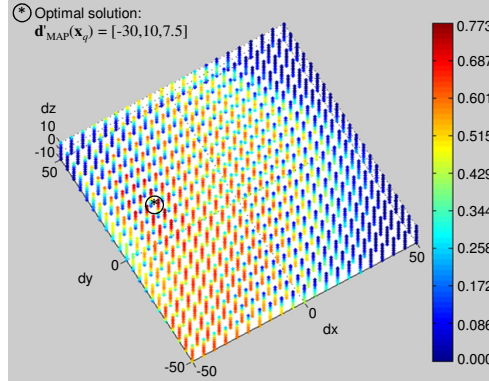


Figure 7: The likelihood associated with each displacement vector in the parameter space. The optimal solution (see asterisk) represents the consensus amongst sample estimates $\mathbf{d}_{\text{MAP}}(\mathbf{x}_p)$ in the neighborhood of \mathbf{x}_q , $\mathcal{N}_{\mathbf{x}_q}$

2.3 Complexity

The main computational complexity lies in step 5 of the algorithm. Looking at $L_{m,k} = \sum_g L(y(\mathbf{c}_m) | g) R(\mathbf{x}_m + \mathbf{d}_{m,k}, g, \delta_m)$, since $L(y(\mathbf{c}_m) | g)$ amounts to an $O(1)$ lookup operation, the per-sample complexity comes from $R(\mathbf{x}_m + \mathbf{d}_{m,k}, g, \delta_m)$ where sample m is fixed and $k \in \{1, \dots, N_{\text{displacement}}\}$ varies over the displacement search space. Assuming a rectilinear, uniformly quantized search space over a lattice $\mathcal{L} \subset \mathbb{R}^3$ and n grid points in each linear dimension, an exhaustive brute-force search (see Fig. 8a) is $O(n^3)$.

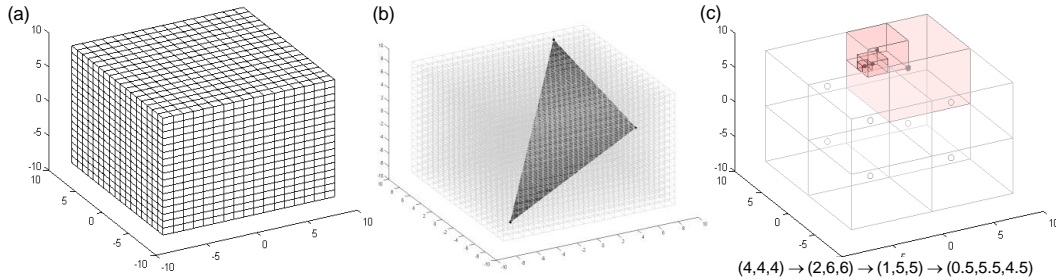


Figure 8: Displacement search space exploration strategies: (a) brute-force, (b) subject to autoregressive or motion predictive modelling constraints, (c) hierarchical approach.

Depending on the surface geometry and sampling density, if the displacement estimation process is amenable to autoregressive or motion predictive modelling [33, 34], complexity drops to $O(n^2)$. As an example, if the optimal displacement at three points in the vicinity of \mathbf{x}_m are represented by the vertices of the triangle in the solution space in Fig. 8(b) and the cost function is locally convex, then the search may be constrained to the triangular region $\Omega \subset \mathbb{R}^2$. Although this paper does not mandate a specific implementation, it is worth noting that a hierarchical search strategy (see k -step successive refinement in Fig. 8c or [35]) has an approximate complexity of $O(n \log n)$ since an $(2^3 + 1)$ point search is conducted k times, where $k \in \mathbb{Z} \approx \log_2 n$.

¹¹In step 7a, the update equation $\mathbf{x}'_q \leftarrow \mathbf{x}_q - \mathbf{d}'_{\text{MAP}}(\mathbf{x}_q)$ contains a minus sign because the displacement error estimation process considers moving samples around the initial boundary. In practice, we need to do the opposite, viz. move the boundary with respect to the samples which remain fixed at their measured locations.

3 Performance evaluation

The benefits of spatial warping is first demonstrated, this will be followed by results from a large scale validation experiment.

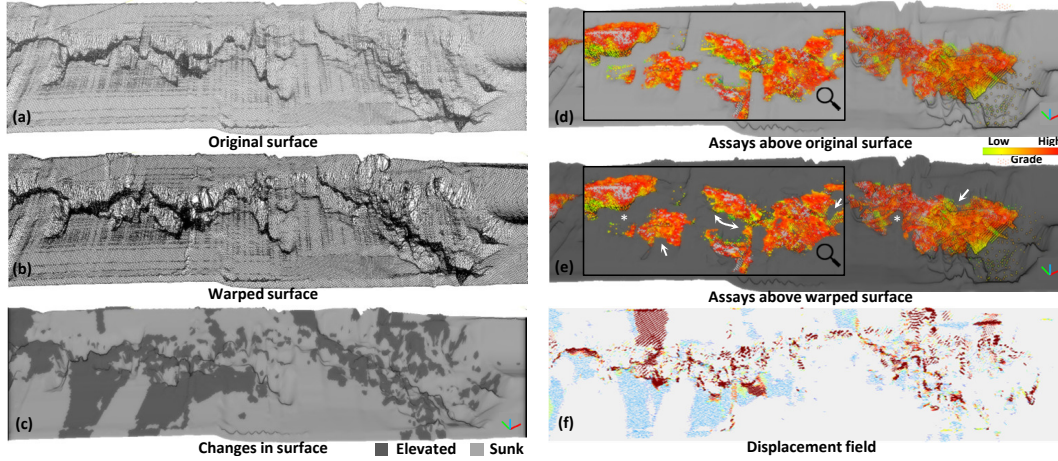


Figure 9: Surface warping performed on a mineralization base surface. (a) original mesh surface, (b) warped surface, (c) map shows where the surface has elevated and sunk after warping. (d)–(e) Assays rendered above the original (resp. warped) surface are predominantly high-grade; (f) displacement field obtained through surface warping (an equivalent high resolution display is shown in Fig. 10)

3.1 Local corrections due to spatial warping

Figure 9 provides an overview of the surface warping result for a mineralization base surface where high grade material ideally sits above the boundary. The bottom panels illustrate the displacement field and highlight changes in elevation by superimposing the surfaces before and after warping. The right hand side panels in the top and middle row show the mineral (Fe) grade of the assay samples situated above the original and warped surfaces.

Figure 10(a) describes the topological changes to the warped surface. It conveys the same information as Fig. 9(c) albeit at higher resolution. This signed distance visualization is generated using a multiscale cloud compare algorithm [36] which takes the original and warped surface vertices as input and displays elevation differences as a color map. Figure 10(b) and insets show the raw displacement field obtained directly from the warping process as a quiver plot.

Figure 11 examines the effects of surface warping in more detail. It provides a magnified view of the rectangular region shown in Fig. 9(d) and (e). As expected, areas pointed by an arrow have contracted after surface warping. This results in the correct behaviour whereby non-mineralized samples have vanished below the mineralization boundary which is implicitly represented by the warped surface. The white lines indicate inclusive behaviour (or areas of expansion) where mineralized samples have risen above the mineralization boundary following surface warping. Overall, local delineation between high-grade and low-grade material has improved. The surface has effectively been pushed down to include more mineralized (red) samples and lifted up to exclude more low-grade (yellow) samples. Although the assay samples are coloured by iron grade alone in this illustration, it is worth bearing in mind that ore grade is assessed in practice as a function of multiple chemical components and this often includes Al_2O_3 and other trace elements.

Figure 12 presents an alternative view. Surface cross-sections (the shell being visualized as black ribbons) are shown together with assay samples (coloured by grade) at two different elevations. Local changes are indicated by the arrows. The original surface is inaccurate at (a.1) as it excludes certain high-grade samples whereas in (a.2), (a.3) and (b.4) waste samples are included inside the boundary. Evidently, the warped surface provides better delineation between waste and high-grade samples as the boundary encircles the waste; this is especially noticeable at (b.4) in the warped surface. These observations can be verified quantitatively in Table 1 which demonstrates more effective separation of high grade and waste samples with warping.¹²

¹²Note that the dominant samples (HG/BL above the surface, and LG/W below the surface) do not quite reach 100%. In part, this is due to some assay samples being taken from hole intervals that span across mineralized and non-mineralized geozones. Other surfaces that further delineate HG and W materials are not considered for the purpose of this evaluation.

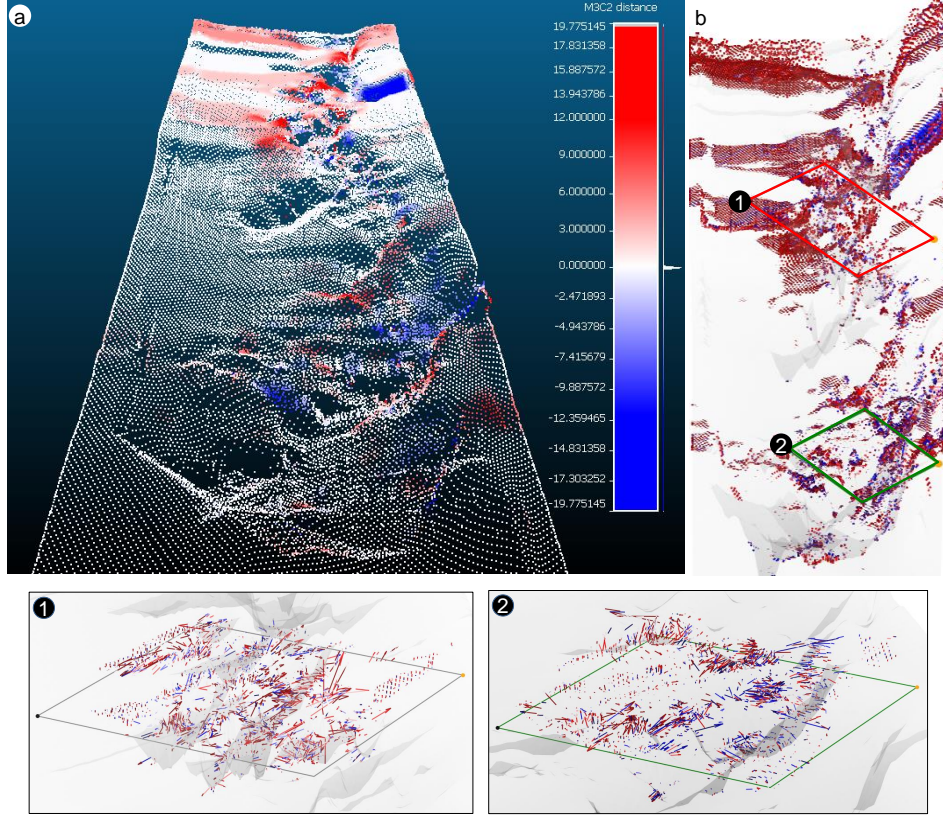


Figure 10: Changes to the surface: (a) signed distance visualization obtained from (b) vertices displacement field; (c)–(d) magnified view of the displacement field in two sub-regions.

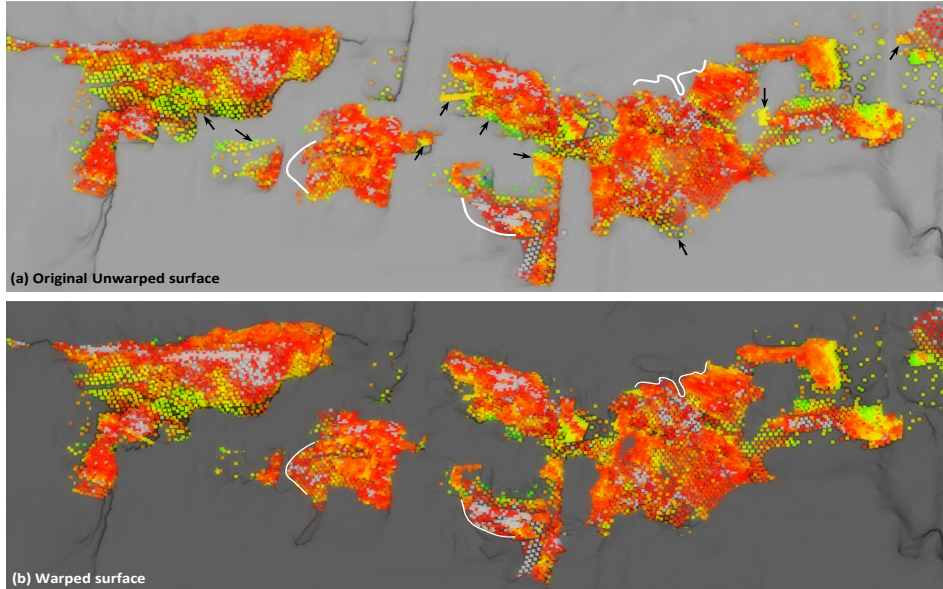


Figure 11: Fe grade of assay samples situated above the (top) original and (bottom) warped 'min_base' surface.

3.2 Validation experiment

To provide an objective evaluation, an end-to-end validation procedure known as r_2 spatial reconciliation is applied to assess the potential benefits of the proposed scheme where surface warping, block model restructuring and interval

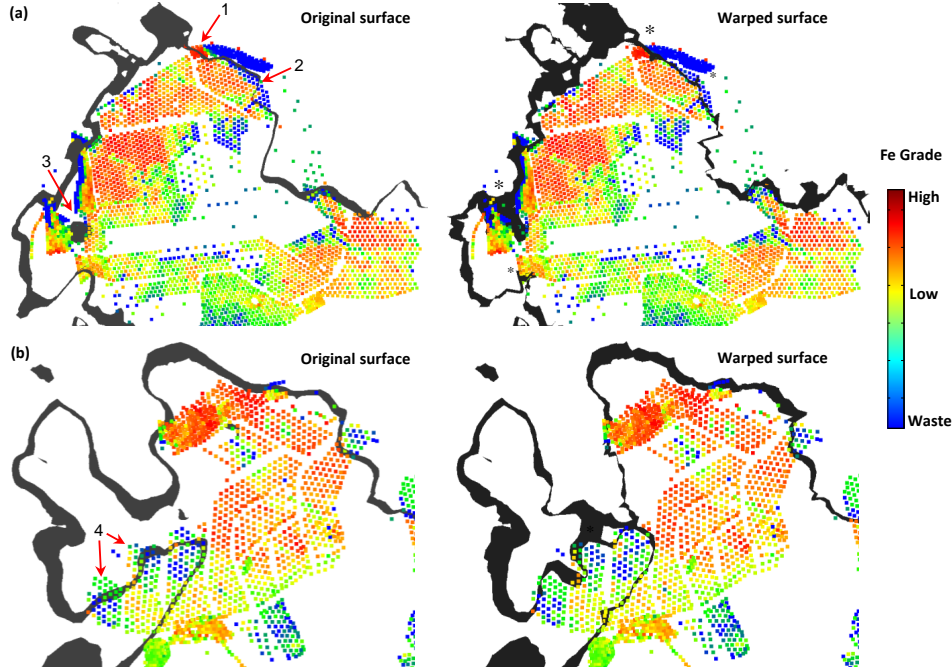


Figure 12: Surface cross-sections taken at (a) $400 \pm 5\text{m}$ and (b) $440 \pm 5\text{m}$ show better delineation between waste and high-grade samples after warping.

Table 1: Assay samples above and below the original and warped surfaces, categorised by High grade (HG), Blended (BL) siliceous and aluminous, Low grade (LG) and Waste (W).

Samples located above surface										
Surface	HG	BLS	BLA	LGS	LGA	W ₁	W ₂	W ₃	$\frac{(HG+BL)}{(HG+BL+LG+W)}$	$\frac{(HG+BL)}{(HG+BL+W)}$
original	12809	1609	3127	714	884	2588	1899	113	73.8%	79.2%
warped	13421	1730	3286	710	975	2194	1968	145	75.5%	81.0%
change	+++++	+	++		+	----	+		+1.7%	+1.8%
Samples located below surface										
Surface	HG	BLS	BLA	LGS	LGA	W ₁	W ₂	W ₃	$\frac{(LG+W)}{(HG+BL+LG+W)}$	$\frac{(W)}{(HG+W)}$
original	1396	723	553	513	558	3874	876	223	69.3%	78.0%
warped	783	602	394	518	468	4268	806	191	77.8%	87.1%
change	-----	-	--		-	++++	-		+8.5%	+9.1%

GP grade inferencing are applied, relative to a baseline resource model where none of these are used. The comparison requires computing r_2 values or ratios of (grade-block average)/(model predicted value) for each respective model and a chemical of interest, where a “grade-block” is an industry term that refers to regions with fairly constant composition and a typical volume ranging from 625 m^3 to $145,000\text{ m}^3$. These grade-blocks are marked with a destination tag for mining excavation purpose based on material types and/or the estimated grades. The grade-block averages (for Fe, SiO_2 etc.) are computed by geologists using the blast hole assays contained within the grade-block boundaries. The corresponding model predictions are volume-weighted averages of the GP inferenced mean grade values calculated over all blocks (perhaps numbered in the tens, hundreds or thousands) that intersect with each grade-block.¹³

Table 2 shows the raw data for 5 grade-blocks and r_2 values computed for the proposed and reference model. Each grade-block is identified by the pit, bench and destination-tag. What is shown is only a snippet of a large table. The dest-tags¹⁴ represent a classification based on average grade-block composition. For validation, we will consider two pits (A and B) from a Pilbara iron ore mine and five benches each of height 10m with a base elevation from 70m to

¹³Fair sampling — whether the number of samples taken is adequate and representative of the geology — is an important consideration from the viewpoints of reliability and performance evaluation. In reality, suboptimal sampling does occur particularly in low-grade regions where the cost of extra sampling outweighs the benefit of knowing more about a waste zone with zero profit potential. In any event, the grade-block averages are as close to the ground truth as one can possibly attain.

¹⁴HG = high grade, WH = waste/hydrated, BGA = blended aluminous, LGS = low grade siliceous.

110m in 10m increment. In Table 2, bench 90 extends from a height of 90m to 100m. Accordingly, the grade-blocks used for evaluation are restricted to this z-interval. Model performance will be evaluated in ‘intra-bench’ and ‘predictive’ mode. The former, indicated by RL_{90} for instance, allows data down to a minimum elevation of 90m to be used during modelling (incl. GP training). Evaluation of an RL_{90} model on bench 90 indicates how well a model interpolates the assay data. The latter, indicated by RL_{100} , permits only data down to 100m to be used during modelling. Evaluation of an RL_{100} model on unseen data from bench 90 focuses on a model’s look-ahead (generalization and prediction) capability, viz. how well it vertically extrapolates the assay data. These differences are illustrated in Fig. 13.

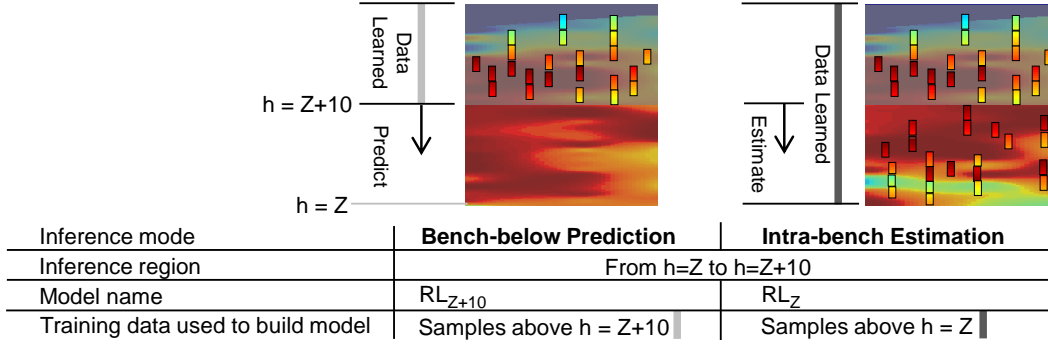


Figure 13: Model evaluation inferencing modes. (Left) bench-below / forward prediction, (right) intra-bench estimation mode.

Table 2: r_2 spatial reconciliation: excerpt of raw data showing the grade-block (gb) and model predicted averages and normalized tonnage associated with 5 grade blocks.

Pit/ bench/ blast# / dest-tag	tonne%	Fe (gb)	Fe (model)	Fe r_2	SiO ₂ (gb)	SiO ₂ (model)	SiO₂ r_2	Al ₂ O ₃ (gb)	Al ₂ O ₃ (model)	Al₂O₃ r_2
Proposed model										
A/90/1/HG13	1.47028	63.558	63.679	0.998	2.281	2.219	1.027	1.977	1.892	1.045
A/90/1/WH10	0.90878	47.969	54.935	0.873	25.786	14.664	1.758	1.762	2.022	0.871
A/90/3/HG23	1.25085	62.237	59.237	1.050	3.834	7.195	0.532	2.011	1.758	1.143
A/90/399/BGA9	0.73250	56.618	55.832	1.014	8.807	9.748	0.903	3.034	3.228	0.940
A/90/5/LGS40	0.95260	54.531	52.953	1.029	9.440	10.383	0.909	6.853	7.581	0.904
Reference model										
A/90/1/HG13	1.53145	63.558	62.942	1.009	2.281	2.640	0.863	1.977	2.098	0.942
A/90/1/WH10	0.89634	47.969	56.863	0.843	25.786	11.948	2.158	1.762	2.048	0.860
A/90/3/HG23	1.13243	62.237	63.299	0.983	3.834	2.434	1.575	2.011	2.061	0.975
A/90/399/BGA9	0.63901	56.618	51.399	1.101	8.807	16.487	0.534	3.034	3.301	0.919
A/90/5/LGS40	0.94149	54.531	56.785	0.960	9.440	8.183	1.153	6.853	5.719	1.198

In order to convey useful information for large-scale performance evaluation, we propose using an r_2 error score. First, the r_2 values associated with bench z and an RL_h model (where $h = z$ in intra-bench mode, or $h = z + 10$ in predictive mode) are sorted in increasing order and cumulative tonnage percentages are computed. This produces an r_2 cumulative distribution function (cdf); an example of which is shown in Fig. 14(a). An r_2 value less than 1 indicates over-estimation by the model, conversely, a value greater than 1 indicates under-estimation w.r.t. the grade-blocks. In a perfect scenario where there is zero discrepancy between the grade-blocks and model predicted values, the cdf curve becomes a step function that transitions from 0% to 100% at an r_2 value of 1. Hence, adding the area below the curve for $r_2 < 1$ to the area above the curve for $r_2 \geq 1$ provides an aggregate error measure (a performance statistic) of a model for a given pit, bench and chemical. The graphs also give insight. For instance, the left-leaning red curve in Fig. 14(f) provides evidence of bias, viz. the reference model has a tendency of over-estimating the Al_2O_3 grade in pit B for bench 90.

The two pits combined contain over 400 grade-blocks and a volume in excess of $3 \times 10^6 \text{ m}^3$. The summary statistics for intra-bench estimation and bench-below prediction are shown in Table 3. The main observation is that the proposed model outperforms the reference model. With few exceptions, the r_2 error scores are consistently lower for both intra-bench and bench-below prediction for Fe, SiO_2 and Al_2O_3 . Generally, the error scores are higher for bench-below prediction, the performance gap reflects the relative difficulty of the problem. These findings suggest the use of surface warping, block model spatial restructuring and interval GP inference can increase accuracy in grade estimation. In particular, improving the alignment of mesh surfaces with respect to the underlying boundaries (using

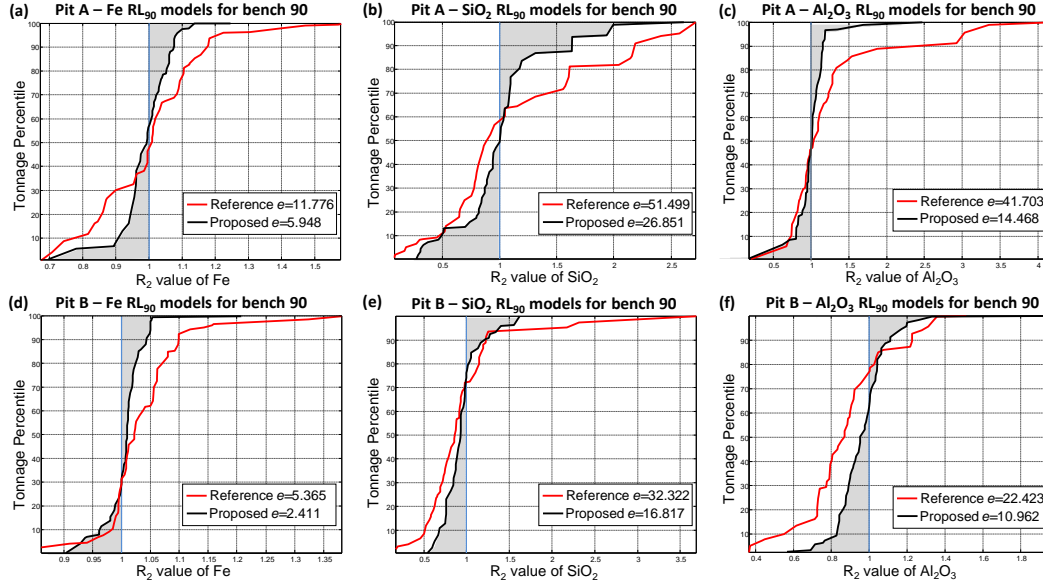


Figure 14: Evaluation of orebody grade estimation RL_{90} model using grade blocks from two pits and bench 90. The r_2 cumulative distribution function associated with pit A (top) and pit B (bottom) are shown from left to right for Fe, SiO_2 and Al_2O_3 .

Table 3: r_2 spatial reconciliation r_2 statistics.

Bench	Model	Pit A						Pit B					
		Proposed model			Reference			Proposed model			Reference		
		Fe	SiO_2	Al_2O_3	Fe	SiO_2	Al_2O_3	Fe	SiO_2	Al_2O_3	Fe	SiO_2	Al_2O_3
Intra-bench estimation performance													
110	RL_{110}	4.271	18.202	12.059	7.761	34.531	19.995	3.351	20.905	17.516	4.069	21.737	20.087
100	RL_{100}	5.411	28.101	24.784	8.548	46.368	29.377	2.093	15.670	11.505	3.282	22.298	19.057
90	RL_{90}	5.948	26.851	14.468	11.776	51.499	41.703	2.411	16.817	10.962	5.365	32.322	22.423
80	RL_{80}	4.693	16.172	21.967	12.182	60.436	27.069	6.777	22.986	18.957	10.461	39.828	29.820
70	RL_{70}	9.420	19.646	25.036	11.135	49.092	53.319	9.416	24.409	44.289	9.688	39.862	77.711
μ_g		5.711	21.280	18.828	10.117	47.611	31.816	4.042	19.862	17.933	5.919	30.140	28.823
Bench-below prediction performance													
100	RL_{110}	6.707	41.035	34.372	8.548	46.372	29.381	4.136	20.800	25.621	3.282	19.060	22.301
90	RL_{100}	9.832	41.214	26.107	11.776	51.495	38.455	4.100	29.440	17.766	5.365	32.322	22.425
80	RL_{90}	7.336	24.695	21.196	12.182	60.437	27.067	8.794	29.516	27.742	10.461	39.821	29.817
70	RL_{80}	8.069	28.985	42.950	11.135	49.097	53.319	9.605	25.907	63.121	9.688	39.859	77.786
μ_g		7.904	33.170	30.064	10.810	51.594	35.734	6.152	27.558	28.362	6.500	32.705	31.554

μ_g denotes the geometric mean

the observed geochemistry from samples to enforce consistency) can make a real difference and improve orebody modelling outcomes.

3.3 Discussion

Although the results have been analyzed in the context of improving grade models, there is also intrinsic value in updating geological boundaries via surface warping using geochemical assay data. The ability to better characterize the lithological contacts (e.g. transition between mineralized and unmineralized domains) improves the mine geologist's ability to understand ore genesis events, particularly fluid flow within major structures in a banded iron formation (BIF) hosted iron ore system [37, 38]. Shale boundaries¹⁵, along with folds and faults, play a significant role in controlling mineralization as fluid pathways are restricted by impermeable layers such as shale bands.

¹⁵Shale is essentially a clay mineral with elevated SiO_2 and Al_2O_3 content.

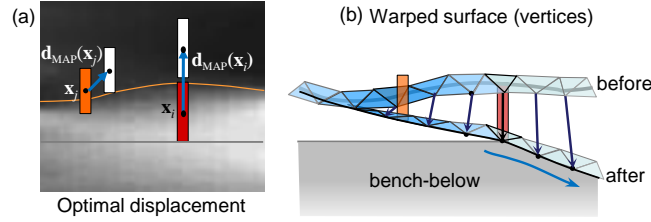


Figure 15: Surface warping can propagate directional information about a boundary to the bench below

From a modelling perspective, warped surfaces have been used successfully to modify the block model structure in [25] to improve the delineation between domains for grade estimation. Commercially available geo-modelling softwares often employ implicit modelling techniques [39] to extract boundary as an iso-surface from a manifold. Recent work by Renaudeau et al. even handles discontinuities [40]. A recognized problem with this process is that it generally assumes the entire dataset is available and models everything at once. In contrast, our proposal honors the geologist’s interpretations and uses the mesh surfaces prepared by experts as starting points. The warping procedure can be applied iteratively as more production data (for instance, blasthole assays from a single bench) become available to rectify surfaces incrementally. This flexible approach works well with sparse data and periodic updates which underscore the progressive nature of open-pit mining.

More accurate knowledge about these geological boundaries can be exploited to improve decision making and process efficiency. It facilitates dynamic mine planning and presents options on whether to excavate, postpone or abandon operations in an area. Then, there is the fleet management and task scheduling aspect which coordinates the movement of mining equipment [41] such as diggers, excavators and haul trucks, directing them when and where to go to achieve flow targets [42]. Knowing where an ore/waste transition might occur, drill-charge-and-blast operations may be optimized with respect to placement and depth. The directional information conveyed by the surfaces also provides guidance for adaptive sampling [43] which maximizes utility and minimizes cost. This allows specific areas to be targeted where the boundary transition is most uncertain.

As Fig. 15 shows, surface warping can project information to an adjacent bench or the bench below; this gives to some extent a forward stratigraphic modelling capability, allowing the drilling density and assay sampling rate to be adjusted if needed. Geological risks [44] can be mitigated with an improved grade model. These risks include identifying sticky or hazardous material, as well as grade control in general, such as finding waste instead of ore in a variable grade block.

4 Conclusion

This paper described the importance of having an accurate surface for grade estimation in mining. As motivation, it was shown that an inaccurate surface — one that fails to capture the location and shape of the underlying geological boundary — can impact the block structure and inferencing ability of the resultant grade estimation model which in turn can lead to smearing and misleading interpretations. The main contribution was a Bayesian formulation of the surface warping problem which seeks to maximize the agreement between the surface and observed data. The objective was to reshape the surface where possible to provide a clear delineation between ore and waste material that is consistent with the observations. This involved estimating and applying the optimal displacement to the mesh vertices based on spatial and compositional analysis. The maximum a posteriori (MAP) solution considered the chemistry observation likelihood in a given geozone and incorporated an a priori spatial structure which allows the likelihood of a displacement estimate to be computed using geological domain knowledge. The results showed that locally, the mineralized and non-mineralized samples are better separated by the warped surface.

For end-to-end performance evaluation which encompasses surface warping, block model spatial restructuring, and grade estimation based on GP inferencing, the r_2 reconciliation error score was proposed. This provided a grade model validation metric that is useful irrespective of the actual algorithms/processes deployed in the system components. Our experiments showed the r_2 error scores were consistently and significantly lower with surface warping when the estimated grades for chemicals of interest (Fe, SiO₂ and Al₂O₃) were compared with over 400 grade-blocks for two large pits, having a total volume in excess of 3×10^6 m³. This demonstrated the value of implementing the displacement estimation framework for surface warping/boundary rectification, and spatial algorithms more generally, in a mining automation context.

5 Authorship statement

The first two authors contributed to the core contents in this paper. Alexander Lowe studied surface warping (mesh vertices displacement estimation) as a maximum likelihood problem. He investigated different strategies and provided a concrete software implementation. Raymond Leung reformulated the problem in a Bayesian framework, developed the block model spatial restructuring algorithms, and proposed using the R_2 CDF error score as a validation measure. He conceptualized this paper and wrote the manuscript in consultation with other authors. Anna Chlingaryan and Arman Melkumyan devised the covariance functions and mathematical framework for grade estimation and GP inference using interval data (see Appendix). John Zigman conducted the validation experiments. John and Raymond performed data analysis and interpreted the results.

A Appendix: Gaussian Processes — inferencing for grade estimation

Inferencing refers to the task of predicting the grade value for certain chemicals of interest at locations where direct assay measurements are unavailable. In this exposition, Gaussian Process (GP) is used to provide a probabilistic model of the grade functions given a set of data, this allows both the mean and uncertainty associated with the compositional percentage of various chemicals such as Fe, SiO₂ etc. to be estimated. Inferencing is generally preceded by a training phase which optimizes the hyper-parameters that describe the Gaussian Process.

Mathematically, a GP is an infinite collection of random variables, any finite number of which has a joint Gaussian distribution. Machine learning using GPs consists of two steps: training and inference. For training, simulated annealing and gradient descent procedures are used to optimize the hyper-parameters to create a probabilistic model that best represents the training data. Specifically, the GP hyper-parameters include *length scales* that describe the rate of change in composition with space, and *noise variance* that describes the amount of noise present in the data.

A training set $\mathcal{T} = (X, \mathbf{y})$ consists of a matrix of training samples $X = [x_1, x_2, \dots, x_N]^T \in \mathbb{R}^{N \times D}$ and corresponding target vector $\mathbf{y} = [y_1, y_2, \dots, y_N] \in \mathbb{R}^N$. Here, N represents the number of training samples available for a geozone. Each $x_i \in \mathbb{R}^D$ denotes an observation (the spatial coordinates where an assay sample is taken) and the associated value $y_i \in \mathbb{R}$ denotes a chemical's compositional percentage. The objective is to compute the predictive distribution $f(x_*)$ at various test points x_* . Formally, a GP model places a multivariate Gaussian distribution over the space of function variables $f(x)$, mapping input to output spaces. GPs can also be considered as a stochastic process that can be fully specified by its mean function $m(x)$ and covariance function $k(x, x')$. To completely describe the standard regression model, we assume Gaussian noise ε with variance σ_n^2 , so that $y = f(x) + \varepsilon$. With a training set $(X, f, y) = (\{x_i\}, \{f_i\}, \{y_i\})_{i=1:N}$ and test set $(X, f, y) = (\{x_{*i}\}, \{f_{*i}\}, \{y_{*i}\})_{i=1:N}$ where $\{y_i\}$ are observed and $\{y_{*i}\}$ are unknown and $m(x) = 0$, the joint distribution becomes

$$\begin{bmatrix} y \\ f_* \end{bmatrix} \sim \mathcal{N} \left(0, \begin{bmatrix} K(X, X) + \sigma_n^2 I & K(X, X_*) \\ K(X_*, X) & K(X_*, X_*) \end{bmatrix} \right) \quad (10)$$

In Equation (10), $\mathcal{N}(\mu, \text{cov}(f_*))$ is a multivariate Gaussian distribution with mean μ , posterior covariance at the estimated locations $\text{cov}(f_*)$, and K is the covariance matrix computed between all the points in the set. Thus, the matrix element $K_{i,j*} \equiv K(X_i, X_{*j})$ for instance is obtained by applying the kernel to the locations of sample x_i and x_{*j} from the training and test sets, respectively. By conditioning on the observed training points, the predictive distribution for new points can be obtained as:

$$p(f_* | X_*, X, y) = \mathcal{N}(\mu, \text{cov}(f_*)) \quad (11)$$

where

$$\mu = K(X_*, X) [K(X, X) + \sigma_n^2 I]^{-1} y \quad (12)$$

and the posterior covariance

$$\text{cov}(f_*) = K(X_*, X_*) - K(X_*, X) [K(X, X) + \sigma_n^2 I]^{-1} K(X, X_*) \quad (13)$$

Learning a GP model is equivalent to learning the hyper-parameters of the covariance function from a data set. In a Bayesian framework, this can be performed by maximising the log of the marginal likelihood [45] with respect to θ :

$$\log p(y | X, \theta) = -\frac{1}{2} y^T [K(X, X) + \sigma_n^2 I]^{-1} y - \frac{1}{2} \log |K(X, X) + \sigma_n^2 I| - \frac{N}{2} \log 2\pi \quad (14)$$

The marginal likelihood is a non-convex function, thus only local maxima can be obtained. It has three terms (from left to right) that represent the data fit, complexity penalty (to include the Occam's razor principle) and a normalization

constant. In this standard framework, the main contribution is the design of new kernels [46] that deal with not only point-based observations, but also *interval* observations where y_i represents an average assay value measured over some interval in drilled holes. This enables performing data fusion between exploration and blast hole assays taking into consideration their respective supports. The GP covariance functions for interval data are described mathematically in [46]. Relevant works that underpin this theory can be found in [47] and [48].

Acknowledgment

This work was supported by the Australian Centre for Field Robotics and the Rio Tinto Centre for Mine Automation.

References

- [1] Francesco Guglielmino, Marco Anzidei, Pierre Briole, Panagiotis Elias, and Giuseppe Puglisi. 3D displacements maps of the 2009 L'Aquila earthquake (Italy) by applying the SISTEM method to GPS and DInSAR data. *Terra Nova*, 25(1):79–85, 2013.
- [2] Warren J Mead. Notes on the mechanics of geologic structures. *The Journal of Geology*, 28(6):505–523, 1920.
- [3] Ravi Krishnamurthy, Pierre Moulin, and John Woods. Optical flow techniques applied to video coding. In *Proceedings, International Conference on Image Processing*, volume 1, pages 570–573. IEEE, 1995.
- [4] Michael M Chang, A Murat Tekalp, and M Ibrahim Sezan. Simultaneous motion estimation and segmentation. *IEEE Transactions on Image Processing*, 6(9):1326–1333, 1997.
- [5] William R Mark, Leonard McMillan, and Gary Bishop. Post-rendering 3D warping. *Symposium on Interactive 3D graphics (SI3D)*, 97:7–16, April 1997.
- [6] Gunnar Farneback. Very high accuracy velocity estimation using orientation tensors, parametric motion, and simultaneous segmentation of the motion field. In *Proceedings Eighth IEEE International Conference on Computer Vision. ICCV 2001*, volume 1, pages 171–177. IEEE, 2001.
- [7] Andrew Secker and David Taubman. Lifting-based invertible motion adaptive transform (LIMAT) framework for highly scalable video compression. *IEEE transactions on image processing*, 12(12):1530–1542, 2003.
- [8] Andrew Nealen, Matthias Müller, Richard Keiser, Eddy Boxerman, and Mark Carlson. Physically based deformable models in computer graphics. In *Computer Graphics Forum*, volume 25, pages 809–836. Wiley Online Library, 2006.
- [9] Olga Sorkine, Daniel Cohen-Or, Yaron Lipman, Marc Alexa, Christian Rössl, and H-P Seidel. Laplacian surface editing. In *Proceedings of the 2004 Eurographics/ACM SIGGRAPH Symposium on Geometry Processing*, pages 175–184. ACM, 2004.
- [10] Jeff B Allan, Brian Wyvill, and Ian H Witten. A methodology for direct manipulation of polygon meshes. In *New Advances in Computer Graphics*, pages 451–469. Springer, 1989.
- [11] Christoph Stiller. Object-oriented video coding employing dense motion fields. In *Proceedings of ICASSP'94. IEEE International Conference on Acoustics, Speech and Signal Processing*, pages V–273. IEEE, 1994.
- [12] Mario Botsch, Leif Kobbelt, Mark Pauly, Pierre Alliez, and Bruno Lévy. *Polygon mesh processing*. AK Peters/CRC Press, 2010.
- [13] Bert De Waele, Mathieu Lacorde, Michael Cunningham, and Benjamin Jupp. Understanding geology and structure: An essential part of mineral resource estimation. *ASEG Extended Abstracts*, 2018(1):1–8, 2018.
- [14] Guillaume Caumon, PLCD Collon-Drouaillet, C Le Carlier De Veslud, S Viseur, and J Sausse. Surface-based 3D modeling of geological structures. *Mathematical Geosciences*, 41(8):927–945, 2009.
- [15] Paul M Thompson and Arthur W Toga. Warping strategies for intersubject registration. In *Handbook of Medical Imaging*, pages 569–601. 2000.
- [16] Raymond Leung. Subsurface boundary geometry modeling: Applying computational physics, computer vision, and signal processing techniques to geoscience. *IEEE Access*, 7:161680–161696, 2019 [Available at: arXiv:2006.03752].
- [17] Jin Huang, Xiaohan Shi, Xinguo Liu, Kun Zhou, Li-Yi Wei, Shang-Hua Teng, Hujun Bao, Baining Guo, and Heung-Yeung Shum. Subspace gradient domain mesh deformation. In *ACM SIGGRAPH 2006 Papers*, pages 1126–1134. 2006.

- [18] Wenzel Jakob, Marco Tarini, Daniele Panozzo, and Olga Sorkine-Hornung. Instant field-aligned meshes. *ACM Trans. Graph.*, 34(6):189–1, 2015.
- [19] Zhiyang Huang and Tao Ju. Extrinsically smooth direction fields. *Computers & Graphics*, 58:109–117, 2016.
- [20] Felix Knöppel, Keenan Crane, Ulrich Pinkall, and Peter Schröder. Globally optimal direction fields. *ACM Transactions on Graphics (ToG)*, 32(4):1–10, 2013.
- [21] Hugo KH Olierook, Richard Scalzo, David Kohn, Rohitash Chandra, Ehsan Farahbakhsh, Chris Clark, Steven M Reddy, and R Dietmar Müller. Bayesian geological and geophysical data fusion for the construction and uncertainty quantification of 3D geological models. *Geoscience Frontiers*, 12(1):479–493, 2021.
- [22] Philippe Calcagno, Jean-Paul Chilès, Gabriel Courrioux, and Antonio Guillen. Geological modelling from field data and geological knowledge: Part i. modelling method coupling 3d potential-field interpolation and geological rules. *Physics of the Earth and Planetary Interiors*, 171(1-4):147–157, 2008.
- [23] Jay M Ver Hoef and Ronald Paul Barry. Constructing and fitting models for cokriging and multivariable spatial prediction. *Journal of Statistical Planning and Inference*, 69(2):275–294, 1998.
- [24] KE MacCormack, RC Berg, H Kessler, HAJ Russell, and LH Thorleifson. Synopsis of three-dimensional geological mapping and modelling at geological survey organizations. *Alberta Geological Survey, Special Report*, 112, 2019.
- [25] Raymond Leung. Modelling orebody structures: Block merging algorithms and block model spatial restructuring strategies given mesh surfaces of geological boundaries. *Journal of Spatial Information Science*, 21:137–174, 2020 [Available at: arXiv:2001.04023].
- [26] Peter Filzmoser and Karel Hron. Outlier detection for compositional data using robust methods. *Mathematical Geosciences*, 40(3):233–248, 2008.
- [27] Robert G. Garrett, Clemens Reimann, Karel Hron, Petra Kynčlová, and Peter Filzmoser. Finally, a correlation coefficient that tells the geochemical truth. *Newsletter for the Association of Applied Geochemists*, 176, 2017.
- [28] Michael Greenacre, Eric Grunsky, et al. The isometric logratio transformation in compositional data analysis: a practical evaluation, Economics Working Paper Series. Technical Report 1627, Barcelona Graduate School of Economics, 2019.
- [29] Danielle Robinson, Mehala Balamurali, Arman Melkumyan, Alexander Lowe, Raymond Leung, and Tamara Vasey. Automated updating of geological model boundaries for improved ore extraction (Patent WO2020/124148A1, AU2018/904818). Available at: <https://patents.google.com/patent/WO2020124148A1>. Filed: December 18, 2018, published: June 25, 2020.
- [30] Wenping Gong, Chao Zhao, C Hsein Juang, Huiming Tang, Hui Wang, and Xinli Hu. Stratigraphic uncertainty modelling with random field approach. *Computers and Geotechnics*, 125:103681, 2020.
- [31] X Huang, CM Griffiths, and J Liu. Recent development in stratigraphic forward modelling and its application in petroleum exploration. *Australian Journal of Earth Sciences*, 62(8):903–919, 2015.
- [32] Raymond Leung, Mehala Balamurali, and Alexander Lowe. Surface warping incorporating machine learning assisted domain likelihood estimation: A new paradigm in mine geology modelling and automation. *Mathematical Geosciences (provisionally accepted)*, 2021 [Preprint available at arXiv:2103.03923].
- [33] Ashraf Elnagar and Kamal Gupta. Motion prediction of moving objects based on autoregressive model. *IEEE Transactions on Systems, Man, and Cybernetics-Part A: Systems and Humans*, 28(6):803–810, 1998.
- [34] Eunwoo Kim, Sungjoon Choi, and Songhwai Oh. A robust autoregressive gaussian process motion model using l_1 -norm based low-rank kernel matrix approximation. In *2014 IEEE/RSJ International Conference on Intelligent Robots and Systems*, pages 4396–4401. IEEE, 2014.
- [35] Janusz Konrad. Motion detection and estimation. In Alan C Bovik, editor, *Handbook of Image and Video Processing*, chapter 3.10, pages 253–274. Elsevier Academic Press, 2005.
- [36] Dimitri Lague, Nicolas Brodu, and Jérôme Leroux. Accurate 3d comparison of complex topography with terrestrial laser scanner: Application to the rangitikei canyon (nz). *ISPRS Journal of Photogrammetry and Remote Sensing*, 82:10–26, 2013.
- [37] SG Hagemann, T Angerer, Paul Duuring, CA Rosière, RC Figueiredo e Silva, L Lobato, AS Hensler, and DHG Walde. BIF-hosted iron mineral system: a review. *Ore Geology Reviews*, 76:317–359, 2016.
- [38] Caroline Perring, Matt Crowe, and Jon Hronsky. A new fluid-flow model for the genesis of banded iron formation-hosted martite-goethite mineralization, with special reference to the north and south flank deposits of the hamersley province, western australia. *Economic Geology*, 115(3):627–659, 2020.

- [39] EJ Cowan, RK Beatson, HJ Ross, WR Fright, TJ McLennan, TR Evans, JC Carr, RG Lane, DV Bright, AJ Gillman, et al. Practical implicit geological modelling. In *Fifth International Mining Geology Conference*, pages 17–19. Australian Institute of Mining and Metallurgy Bendigo, Victoria, 2003.
- [40] Julien Renaudeau, Modeste Irakarama, Gautier Laurent, Frantz Maerten, and Guillaum Caumon. Implicit modelling of geological structures: A cartesian grid method handling discontinuities with ghost points. *WIT Transactions on Engineering Sciences*, 122:189–199, 2019.
- [41] M Samavati, AW Palmer, AJ Hill, and KM Seiler. Improvements in plan-driven truck dispatching systems for surface mining. In *Mining goes Digital: Proceedings of the 39th International Symposium 'Application of Computers and Operations Research in the Mineral Industry' (APCOM 2019), June 4-6, 2019, Wroclaw, Poland*, page 357. CRC Press, 2019.
- [42] Konstantin M Seiler, Andrew W Palmer, and Andrew J Hill. Flow-achieving online planning and dispatching for continuous transportation with autonomous vehicles. *IEEE Transactions on Automation Science and Engineering*, 2020.
- [43] Nasir Ahsan, Steven Scheduling, Sildomar T. Monteiro, Raymond Leung, Charles McHugh, and Danielle Robinson. Adaptive sampling applied to blast-hole drilling in surface mining. *International Journal of Rock Mechanics and Mining Sciences*, 75:244–255, 2015.
- [44] Jörg Benndorf and Roussos Dimitrakopoulos. Stochastic long-term production scheduling of iron ore deposits: integrating joint multi-element geological uncertainty. *Journal of Mining Science*, 49(1):68–81, 2013.
- [45] Christopher KI Williams and Carl Edward Rasmussen. *Gaussian processes for machine learning*, volume 2. MIT press Cambridge, MA, 2006.
- [46] Danielle Robinson, Arman Melkumyan, and Anna Chlingaryan. Estimating material properties (Patent WO2014/134655A8, US2016/0033676A1, AU2013/900742). Available at <https://patentimages.storage.googleapis.com/da/2f/01/c94254d3a5a81f/US20160033676A1.pdf>. Filed: March 5, 2013, published: December 4, 2014.
- [47] Arja Jewbali, Fabio T. Ramos, and Arman Melkumyan. A non-parametric Bayesian framework for automatic block estimation. In *Proceedings., APCOM Symposium*, number 056, pages 1–20. AusIMM, 2011.
- [48] Carl Edward Rasmussen and Zoubin Ghahramani. Bayesian monte carlo. *Advances in Neural Information Processing Systems*, pages 505–512, 2003.